ACS OMEGA

Open Access

http://pubs.acs.org/journal/acsodf

Article

Probing Microscale Structuring-Induced Phase Separation with Fluorescence Recovery Diffusion Dynamics in Poly(ethylene glycol) Solutions

Shipra Bhatt, Debjani Bagchi,* Avik Das, Ashwani Kumar, and Debasis Sen

Cite This: *ACS Omega* 2023, 8, 35219−35231

Read Online

ACCESS | Metrics & More | Article Recommendations | Supporting Information

ABSTRACT: Apart from biocompatibility, poly(ethylene glycol) (PEG)-based biomedical constructs require mechanical tunability and optimization of microscale transport for regulation of the release kinetics of biomolecules. This study illustrates the role of inhomogeneities due to aggregates and structuring in the PEG matrix in the microscale diffusion of a fluorescent probe. Comparative analysis of fluorescence recovery after photobleaching (FRAP) profiles with the help of diffusion half-time is used to assess the diffusion coefficient (D). The observations support a nontrivial dependence of diffusion dynamics on polymer concentration (volume fraction, φ) and that of fillers carboxymethyl cellulose (CMC) and nanoclay bentonite (B). D values follow the Rouse scaling $D \sim \varphi^{-0.54}$ in PEG solutions. The diffusion time of the fluorescent probe in the PEG+bentonite matrix reveals the onset of depletion interaction-induced phase separation with an increase in bentonite concentration in the PEG matrix beyond 0.1 wt %. Beyond this concentration, structure factors obtained from prebleach FRAP images show a rapid increase at low Q. The two-phase system (PEG-rich and bentonite-rich) was characterized by the hierarchical structural topology of bentonite aggregates, and aggregate sizes were obtained at different length scales with phase contrast imaging, small-angle neutron scattering, and small-angle X-ray scattering. The microscale transport detection presented captures sensitively the commencement of phase separation in the PEG + bentonite matrix, as opposed to the PEG or PEG + CMC matrix, which are observed to be one-phase systems. This method of diffusion half-time and prebleach image analysis can be used for the fast, high-throughput experimental investigation of microscale mechanical response and its correlation with structuring in the polymer matrix.

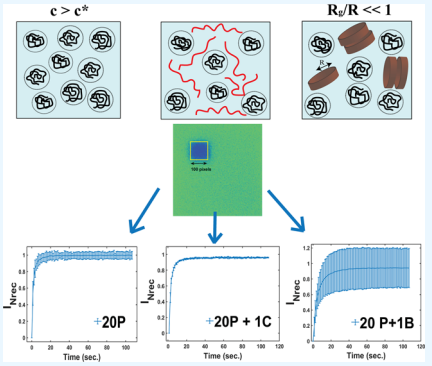

1. INTRODUCTION

Poly(ethylene glycol) (PEG) is a widely used biodegradable polymer for several biomedical applications such as drug delivery, nanomedicine, biodegradable scaffolds for wound healing, or 3D bioprinting of artificial tissues, each requiring tunability of mechanical properties of the PEG matrix.[1−5] For this purpose, fillers such as clay particles, semiflexible cellulose fibers, and carboxymethyl cellulose (CMC) polyelectrolyte are added with cross-linking of the PEG matrix in order to achieve the desired mechanical modifications in PEG with minimal cellular toxicity.[6,7] Nanoparticles can be dispersed in the matrix uniformly or as hierarchical, even percolating, structures on the one hand and as phase-separated domains on the other hand. The mode of dispersion changes the polymer−nanoparticle interface, which can influence polymer conformations and chain dynamics, affecting properties at the macroscale. The structure and dynamics near polymer−nanoparticle interfaces can affect controlled drug release. Hence, study of the dynamical mechanical response at the microscale is imperative for designing application-specific polymer-filler matrices.

Incorporation of fillers such as clay particles in the PEG matrix introduces additional interactions such as depletion interactions and clay-polymer associative networks, which have been observed to modulate stress relaxation.[8−13] In addition, several impediments such as concentration and flow-induced shear banding, yielding, gelation, aging, and microstructuring can arise, necessitating simultaneous measurement of the solution microstructure.[9,13−17] Scattering studies under flow and at rest reveal that structural changes are crucial in understanding mechanical response.[12,13,17−19] Several experimental, theoretical, and simulation studies on nanoparticle-reinforced polymer matrices have revealed a varying degree of mechanical modification of the host polymer matrix by nanoparticles as a result of additional length and time scales introduced due to ineractions.[20−26] In addition, heterogeneities due to competing interactions can prevent mechanical tunability by simple concentration changes of the constituents,

Received: July 9, 2023
Accepted: August 29, 2023
Published: September 14, 2023

Table 1. Length Scales (Entanglement Mesh or Blob Size ξ) and Interaction Strength ($\varnothing_{Dep}$, Depletion Interactions in the Presence of Bentonite) for Different Concentrations of PEG Aqueous Solutions[a]

sample	volume fraction $\varphi = \frac{\frac{c_{pol}}{\rho_{pol}}}{\frac{c_{pol}}{\rho_{pol}} + \frac{(100 - c_{pol})}{\rho_{solv}}}$	$\xi = R_g\left(\frac{\varphi}{\varphi^*}\right)^{-0.76}$ (theoretical in nm)	$\xi = R_g\left(\frac{\varphi}{\varphi^*}\right)^{-0.76}$ (experimental in nm)	$\frac{2R}{\xi}$ (hydrodynamic radius of fluorescein, R = 0.504 nm, ξ from Col 4)	$\frac{R}{R_g}$ (fluorescein)	$\frac{b}{R_g}$ (b = size of bentonite from SAXS = 34 nm)	$\frac{\varnothing_{Dep}}{k_BT} = -\frac{3b}{2R_g}\varphi = -11.86\,\varphi$
5P	0.042	4.58	3.3	0.3	0.116	7.9	0.5
10P	0.085	2.68	2.8	0.36			1.01
20P	0.17	1.56	1.11	0.9			2.02
30P	0.26	1.13	0.8	1.22			3.08
50P	0.46	0.757	0.54	1.86			5.46

[a]The theoretical value of R_g calculated from $R_g = 0.02\ M_w^{0.58}$ = 6.246 nm and its experimental value is 4.3 nm.[51] The critical overlap concentration $\varphi^* = \frac{M_w}{\frac{4}{3}\rho\pi R_g^3 N_A}$ = 0.0289. The volume fraction is calculated from the polymer concentration in wt % (c_{pol}), density of the polymer (ρ_{pol}), and density of the solvent (ρ_{solv}).

Table 2. Results of FRAP Data Analysis for Diffusion Time (τ, From eq 3), Diffusion Half-Time ($t_{1/2}$), Immobile Fraction, and Diffusion Constants (D3) Calculated by eq 5 (Materials and Methods Section)

sample	PEG (wt %)	bentonite (wt %)	CMC (wt %)	τ (s)	$t_{1/2}$ (s)	immobile fraction (M_{If})	$D = \frac{r_n^2 + r_e^2}{8t_{1/2}}$ (μm^2 s^{-1}) (D3)
water	0	0	0	1.02 ± 0.04	0.70 ± 0.03	0	327 ± 15
5P	5	0	0	0.99 ± 0.04	0.68 ± 0.03	0	337 ± 16
10P	10	0	0	1.24 ± 0.07	0.85 ± 0.05	0.018 ± 0.005	270 ± 16
20P	20	0	0	1.736 ± 0.009	1.20 ± 0.06	0.01 ± 0.003	193 ± 10
50P	50	0	0	27.8 ± 0.7	19.2 ± 0.5	0.055 ± 0.007	12 ± 0.3
20P + 0.01B	20	0.01	0	12.2 ± 0.2	8.4 ± 0.1	0.166 ± 0.003	87 ± 1
20P + 0.1B	20	0.1	0	11.1 ± 0.1	7.7 ± 0.1	0.135 ± 0.002	29.9 ± 0.4
20 + 1B	20	1	0	5.7 ± 0.2	4 ± 0.15	0.067 ± 0.003	57 ± 2
0.01B	0	0.01	0	3.8 ± 0.1	2.6 ± 0.1	0.234 ± 0.004	87 ± 4
0.1B	0	0.1	0	3.3 ± 0.1	2.3 ± 0.1	0.25 ± 0.004	98 ± 5
1B	0	1	0	4.44 ± 0.01	3.08 ± 0.07	0.105 ± 0.003	241 ± 5
20P + 0.01C	20	0	0.01	1.7 ± 0.04	1.18 ± 0.03	0.03 ± 0.004	196 ± 5
20P + 0.1C	20	0	0.1	2.06 ± 0.05	1.42 ± 0.04	0.035 ± 0.004	162 ± 4
20P + 1C	20	0	1	2.06 ± 0.06	1.42 ± 0.04	0.049 ± 0.004	162 ± 5
0.01C	0	0	0.01	2.8 ± 0.1	1.9 ± 0.1	0.197 ± 0.003	117 ± 6
0.1C	0	0	0.1	2.4 ± 0.1	1.7 ± 0.08	0.187 ± 0.005	135 ± 6
1C	0	0	1	3 ± 0.1	2.1 ± 0.1	0.237 ± 0.03	108 ± 5

thereby affecting the tribology of films of these nanocomposites, enhancing susceptibility to wear, cavitations, fibrillations, crack formation, and fracture.

This study aims to explore the effect of associative intermolecular interactions between polymer chains and phase separation due to depletion interactions in the presence of colloidal clay particles on microscale dynamics. We analyze the applicability of fluorescence recovery after the photobleaching (FRAP) technique for determining the mechanical response of these solutions at the microscale. Diffusion coefficient values obtained from FRAP are sensitive to the entanglement mesh size of the polymer and reveal the presence of microscale heterogeneities in PEG with an increase in the PEG concentration and the addition of CMC and bentonite. A method to analyze the static solution microstructure is presented and corroborated with small-angle X-ray and neutron scattering data. Small-angle scattering curves of PEG-bentonite solutions show a pronounced low q upturn due to microstructural heterogeneities and bentonite aggregates, which are measured by fitting a hierarchical fractal structuring model and by phase contrast imaging. Depletion interactions in PEG-bentonite systems create nano-/microscale matrix inhomogeneities, which in turn lead to subcompartmental diffusion and a spread in diffusion coefficient values of tracer molecules. For analyzing diffusive processes within microphase-separated domains, the approach of diffusion half-time estimation presented can give a high-throughput transport profile in the system without the need for complicated models.

2. MATERIALS AND METHODS

2.1. Materials. Poly(ethylene glycol) (PEG) of molecular weight 20 000 g/mol was purchased from Alfa Aesar and used without further processing. Aqueous solutions of PEG were prepared by weighing the appropriate amounts of PEG for 5, 10, 20, and 50 wt % solution concentrations (referred to, respectively, as 5P, 10P, 20P, and 50P in the manuscript) and dissolved in deionized water (LOBA Chemicals) by stirring with a magnetic stirrer for about an hour at room temperature, around 30 °C. For the fluorescence microscopy experiments, fluorescein disodium salt (Alfa Aesar) was added to obtain a concentration of 30 μM fluorescein in a PEG solution. Solutions of PEG having 0.01, 0.1, and 1 wt % nanoclay bentonite (Sigma) and carboxymethyl cellulose (sodium salt, 90 000 g/mol molecular weight; degree of substitution = 0.7 carboxymethyl groups per anhydro-glucose unit, from Sigma) were prepared following the procedure mentioned above. To maintain a uniform effect of aging of clay solutions on the experimental data, all samples were prepared 1 day prior to

https://doi.org/10.1021/acsomega.3c04917
ACS Omega 2023, 8, 35219−35231

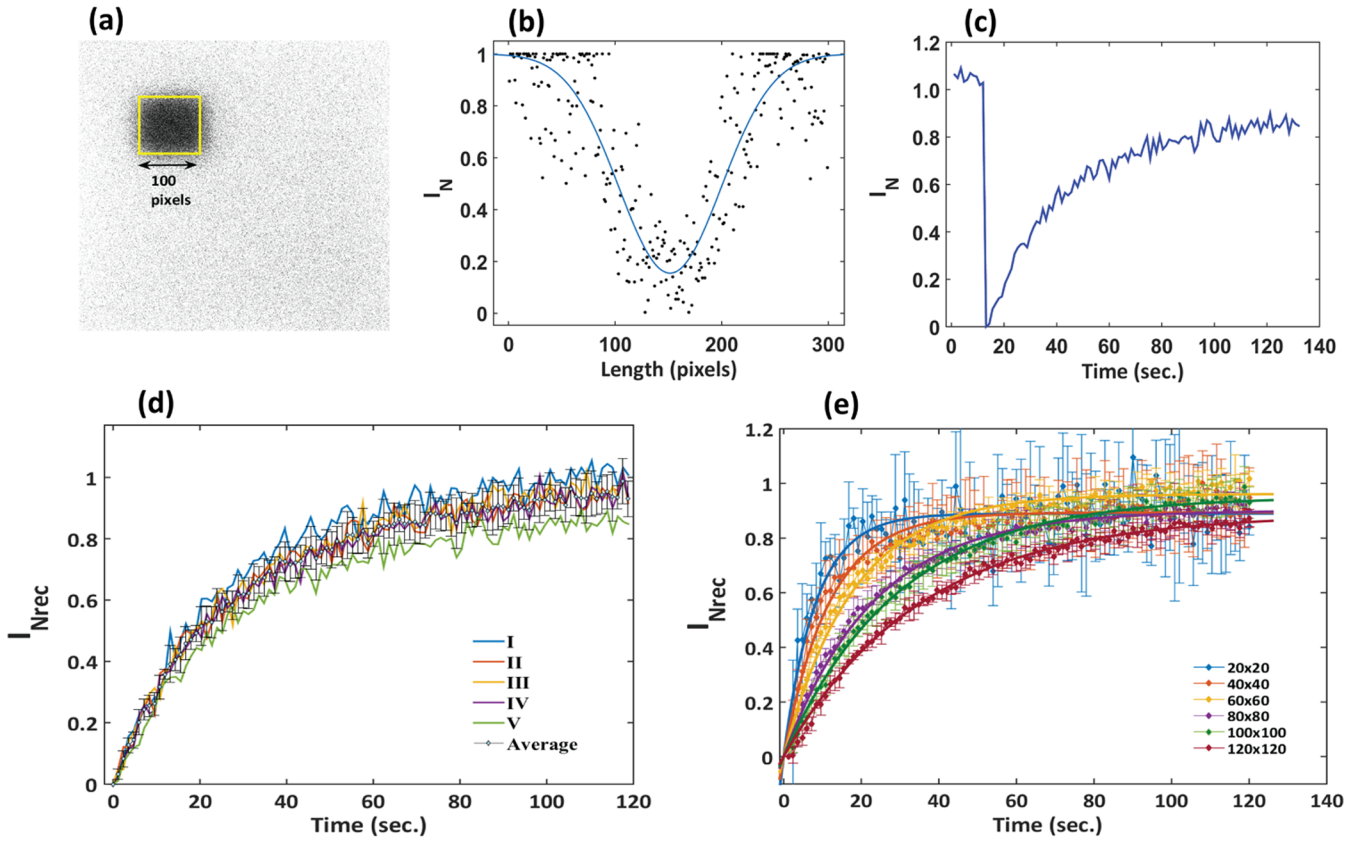

Figure 1. (a) Confocal microscope fluorescence image for the PEG solution with fluorescein, with the bleached spot shown as a dark region, spanning about 100 pixels. (b) The normalized fluorescence intensity profile of the bleached region can be fitted to a Gaussian with spot width w = 96 ± 5 pixels, corresponding to 39.7 ± 2 μm. (c) Typical normalized fluorescence intensity profile obtained, with the prebleach region ($I_N \cong 1$), bleaching ($I_N = 0$), and postbleach regions, showing recovery. (d) FRAP recovery curves obtained after bleaching different regions of the 50 wt % PEG solution. I_{Nrec} is the normalized recovery intensity. (e) FRAP recovery curves for the 50 wt % PEG solution for different sizes of the bleached region given in the inset in pixels.

performing the experiments. All solution concentrations used in performing experiments for different samples are given in Tables 1 and 2, with a nomenclature that will be used throughout the text. The entanglement (or overlap) concentration in volume fraction is calculated as $\varphi^* = 0.0289$ (Table 1), and all investigated volume fractions fall in the semidilute to concentrated polymer solution regimes. Solutions for small-angle neutron scattering experiments were prepared by dissolving the polymers in a deuterated solvent (D_2O). The D_2O was obtained from the BARC heavy water plant at Vadodara, India.

2.2. Fluorescence Recovery after Photobleaching (FRAP). FRAP experiments were carried out with an Olympus IX83 FluoView FV3000 confocal scanning laser microscope (CSLM) with a 60x/1.35 NA Olympus UPLAN APO oil immersion objective. Fluorescence of the fluorescein in the solution was excited with a 488 nm source (OBIS Coherent Laser), and emission was collected at 530 nm in the XY scanning mode of the confocal microscope. For all of the FRAP experiments, the samples were injected into sealed microchannels having a coverslip at one end, which was in contact with the oil immersion objective. 100% laser intensity was used for photobleaching a 100 × 100 pixel region (Figure 1a) in an image of size 512 × 512 pixels (0.414 μm per pixel) for a duration of 2 s. Time-lapse images (~1 s per frame) were acquired before photobleaching and after photobleaching at around 5% laser intensity. This procedure was repeated for five different regions in the microchannel to get an idea of heterogeneities and for statistical accuracy. All FRAP experiments were conducted in a room maintained at 22 °C. Data analysis was performed using custom-made programs in MATLAB. A 512-pixel array line intensity profile was extracted from the center of the bleached spot matrix of the first postbleach image, and a Gaussian fit (eq 1) to this gave a bleach spot width r_e of about 91.3 ± 5 pixels or 37.82 ± 2 μm (Figure 1b).[27]

$$f(x) = 1 - k \exp\left(-\frac{2(x-c)^2}{r_e^2}\right) \quad (1)$$

The total fluorescence intensity of the bleached region of interest (ROI) from prebleach and postbleach images was normalized and corrected for photofading using eq 2[28,29]

$$I_{Nrec}(t) = \frac{I_{data} - I_0}{I_{whole} - I_0} \quad (2)$$

In eq 2, $I_{Nrec}(t)$ is the time-dependent normalized postbleach intensity, I_{data} is the mean intensity of the photobleached region, I_0 is the mean intensity of the photobleached region immediately after bleaching, and I_{whole} is the mean intensity of the entire frame. A typical normalized intensity profile for 50 wt % PEG (50P) is shown in Figure 1c. Unless heterogeneities were studied, the mean of five normalized postbleach profiles was calculated with the standard deviation as the error. This

https://doi.org/10.1021/acsomega.3c04917
ACS Omega 2023, 8, 35219−35231

mean recovery profile was then considered for further analysis. Figure 1d represents the normalized recovery curves for five sets of experiments performed for 50P and the average recovery curve. Figure 1e represents the effect of the size of the bleach ROI, 20 × 20, 40 × 40, 60 × 60, 80 × 80, 100 × 100, and 120 × 120 pixels ROI for 50P on their respective recovery profiles. Most in vitro and in vivo FRAP assays usually have bleach ROI sizes smaller than 50 μm (comparative analysis for different in vitro and in vivo FRAP assays are given in Supporting Table S1) because with an increase in window size, the scanning time increases, leading to flattening of the recovery Gaussian diffusion front and improper estimates of diffusion time. Indeed, FRAP experiments and simulations report large errors in estimation of diffusion coefficients with larger ROIs.[30] Hence, for all of the experiments, the size of the bleach region was chosen subsequently as 100 × 100 pixels (41.4 μm).

In order to calculate diffusion coefficients of the solutions investigated, three different methods were employed and their results were compared. The time-dependent mean normalized recovery profile ($I_{\mathrm{Nrec}}(t)$) after photobleaching was first fitted to eq 3

$$I_{\mathrm{Nrec}}(t) = I_{\infty}(1 - e^{-(t/\tau)}) \tag{3}$$

where τ is the diffusion time and I_{∞} is the intensity at which the FRAP recovery saturates. The results of the fit to eq 3 for different PEG solutions are given in Table 2. However, considering the different nature of interactions present in the different solutions investigated, a single exponential model represented by eq 3 could be an oversimplification.

To circumvent this problem, in the second method, from $I_{\mathrm{Nrec}}(t)$, the half recovery time ($t_{1/2}$) was calculated as the time at which $I_{\mathrm{Nrec}}(t)$ is $0.5I_{\infty}$. In principle, the recovery curve does not reach the prebleach value in most cases due to immobile constituents in the solution, and the immobile fraction is the difference of the recovery curve from the prebleach value. The $t_{1/2}$ can be used to calculate D using eqs 4 and 5[27,31]

$$D = \frac{0.224 r_{\mathrm{n}}^2}{t_{1/2}} \tag{4}$$

$$D = \frac{r_{\mathrm{n}}^2 + r_{\mathrm{e}}^2}{8 t_{1/2}} \tag{5}$$

In the above equations, r_{n} is the actual radius of the photobleached region (50 pixels, or 20.7 μm) and r_{e} is the effective radius of the photobleached region (91.35 pixels, or 37.82 μm), which was calculated by fitting the postbleach recovery profile to a Gaussian (eq 1). The D values calculated from eq 4 (D1) are given in Supporting Table S2, whereas the D values calculated with eq 5 are denoted as D3 and presented in Table 2. D values can also be obtained by fitting the normalized postbleach recovery profiles to eq 6 (D2, Supporting Table S2).[32]

$$I_{\mathrm{Nrec}}(t) = I_{(\infty)}(1 - \sqrt{w^2(w^2 + 4\pi D t)^{-1}}) \tag{6}$$

where $I_{\mathrm{Nrec}}(t)$ is the mean normalized time-dependent postbleach recovery fluorescence intensity, $I_{(\infty)}$ is the asymptotic fluorescence intensity, and w is the half-width of the bleached ROI (20.7 μm). The fit results to eq 6 for FRAP data of all samples are given in Supporting Tables S3 and S4. As a control, FRAP data was collected from an aqueous solution of fluorescein, and the D values computed from eqs 4−6 were compared to the Stokes−Einstein D value of fluorescein in water (with ∼0.5 nm as the hydrodynamic radius of fluorescein in water[43]), which is calculated as 386.2 μm^2 s^{-1} in the present experimental conditions. The D value obtained from eq 5 matches this theoretical D value the best (Table 2). Since the D value calculated with eq 5 (D3, Table 2) gives the best estimate of the fluorescein diffusion coefficient in water in the presently used geometry, the D values are calculated for all of the PEG solutions using eq 5 and compared in the article. The size of the bleach spot and the bleach duration were kept constant for all samples. This estimation of D from the recovery half-time eliminates the need for any model, such as the exponential fit given by eq 3, since a single model may not be valid for all samples.

2.3. Phase Contrast Microscopy. Phase contrast images were captured with a Nikon Eclipse TS100 microscope equipped with a Nikon 40x-0.60NA phase contrast ELWD objective with 300 ms exposure time. The camera used for imaging was a Nikon DS Fi2 with resolution 1 μm/pixel.

2.4. Small-Angle Scattering. In order to probe the hierarchical structure of the polymer-clay nanocomposite in the mesoscopic length scale (i.e., 1−1000 nm), small-angle scattering (SAS) was employed to map the scattering length density fluctuation into the reciprocal space. Here, both small-angle neutron scattering (SANS) and small-angle X-ray scattering (SAXS) measurements[33,34] were carried out on the polymer-clay colloidal dispersion to access a wide range of wave vector transfers, q ($q = 4\pi\sin(\theta)/\lambda$, where "$2\theta$" is the scattering angle and "λ" denotes the wavelength of the probing radiation). SANS measurements were performed using the double-crystal-based medium-resolution SANS facility (MSANS) at GT laboratory, Dhruva reactor, Mumbai, India.[35,36] MSANS probes the lower q domain in the range of 0.003−0.173 nm^{-1} with an incident neutron wavelength of 3.12 Å. The scattered neutron intensities were recorded as a function of q using a 0D BF_3-based neutron detector. The SANS data were corrected for background, transmission, and instrument resolution effects prior to further analysis. The scattering signal at a higher q range (0.06−3.0 nm^{-1}) was accessed using the SWAXS beamline (BL-18) at Indus-2 synchrotron at RRCAT, Indore.[37] The SWAXS beamline, installed at a 5° bending magnet port of the Indus-2 ring, consists of a double-crystal monochromator (DCM) with a pair of Si (111) crystals in a nondispersive geometry and a 1.5 m long toroidal mirror (TM). The DCM was tuned to select 16 keV (λ = 0.765 Å) X-ray photons for carrying out the SAXS measurements. The TM has a coating of 60 nm of Pt and 5 nm of Rh on the silicon substrate to focus the X-ray beam in both sagittal and meridional directions onto the detector plane. The SAXS data were collected using an online image plate area detector (mar345) kept at ∼3.2 m distance from the sample position. The 2D SAXS data were radial-averaged after appropriate transmission and background corrections using an in-house-developed SAXS2D software. Combining both SAXS and SANS scattering signals, a wide q range corresponding to three decades of length scales was accessed.

2.5. Structure Factor and 2D Correlation Calculations. Microscopy gives an idea of the structure and dynamics in real space, whereas scattering gives an idea of structuring in Fourier space, with respect to the scattering wave vector Q. Both of these techniques are complementary, but instrumentation required for simultaneous microscopy and scattering

https://doi.org/10.1021/acsomega.3c04917
ACS Omega 2023, 8, 35219−35231

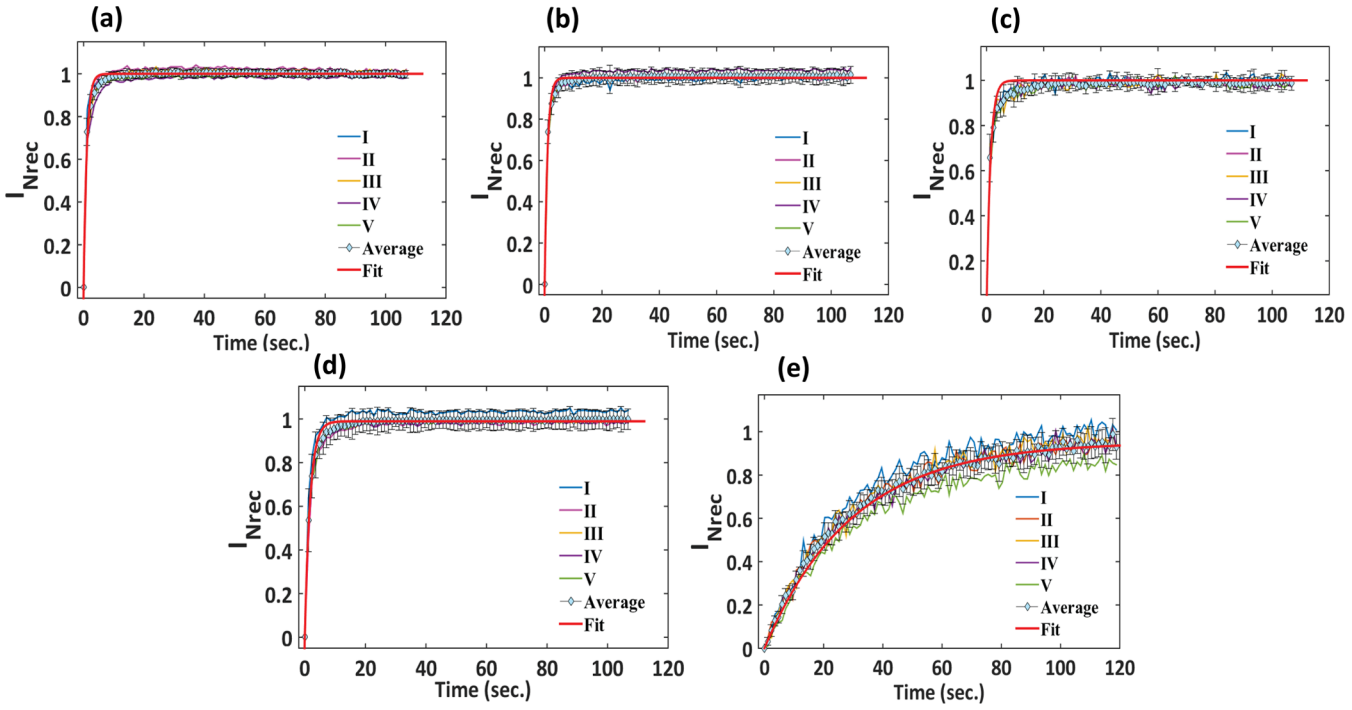

Figure 2. FRAP recovery curves of normalized fluorescence recovery intensity I_{Nrec} as a function of time, for (a) water, (b) 5P solution, (c) 10P solution, (d) 20P solution, and (e) 50P solution, after bleaching five different regions in the sample, with each region represented by Roman numerals I to V. From these curves, the average is calculated and error bars are calculated as the deviation of the curves from the average value. The red curve is the fit with eq 3. The error bars increase with an increase in PEG concentration, and for 20P and 50P solutions, the FRAP curves obtained in different regions have more deviations from the mean curve, with more immobile fractions (Table 2).

experiments is not trivial. This has led in recent years to the development of differential dynamic microscopy (DDM).[38,39] In this method, time series microscopy images are analyzed in Fourier space, using the principles of Fourier optics, removing the requirement of any sophisticated instrumentation. Although it has been used to probe structural dynamics, it results in a very sensitive detection of the static structure factor. If the intensity at a point $\boldsymbol{x}'$ in a microscope image in real space with coordinates (x', y') is represented by $I(\boldsymbol{x}')$, for the image of size $N_x \times N_y$ pixels (=512 × 512 pixels for images in the present case) and magnification M, with l_p (=0.414 μm/pixel in our experiments) being the size of each pixel, then the structure factor, which is the Fourier space (Q-space, Q given by eq 7) representation of $I(\boldsymbol{x}')$, is given as $\tilde{I}(Q)$ (eq 8)[38]

$$Q = \frac{2\pi M}{N_x N_y l_p} \tag{7}$$

$$\tilde{I}(Q) = \sum_p I(x_p') e^{-i(Q \cdot x_p')} \tag{8}$$

In eq 8, the summation is over all of the pixels, p, and $\boldsymbol{x}'$ or (x_p', y_p') is the coordinate of the pth pixel. The above equation was used to calculate the structure factor from the confocal microscopy image of a sample (using the same setup as in FRAP experiments). Since imaging is done with a scanning confocal microscope, each image represents a thin section of the sample, so multiple scattering is negligible and the scattered fluorescence emission of the fluorescein is basically the scattered light captured and the transmitted illuminating beam is eliminated. The final static structure factor $S(Q)$ was obtained by averaging the structure factor (eq 8) obtained from 10 frames for each sample. To calculate the spatial correlations in two dimensions, a convolution was performed over the product of the image intensity matrix in Fourier space and its complex conjugate.

3. RESULTS AND DISCUSSION

3.1. Dynamics of Fluorescent Probes in a Polymer Matrix. A study of diffusion of fluorescent probes in a solution using FRAP can be a sensitive measure of microscale mechanical properties as well as inhomogeneities, if any. This diffusion depends on the size of fluorescent probe particles (R) and the correlation length ξ of the polymer matrix, which characterizes the size of the network formed by overlapping polymer chains in the semidilute regime or the entanglement mesh size.[40] If the particle size is large, so that $\frac{R}{\xi} \gg 1$, then the particle diffusion is a probe of the macroscopic viscosity, as measured by a rheometer. On the other extreme, if $\frac{R}{\xi} \ll 1$, then the particle diffusion is mostly governed by solvent viscosity, as the probes can easily navigate through the empty spaces in the polymer network. The intermediate regime of $\frac{R}{\xi} \sim 1$, where the particles probe the local viscosity of the polymer matrix, can be a sensitive tool to study microscale mechanical properties and heterogeneities.

The intermediate regime was therefore chosen to probe the microscale diffusion of fluorescein probes (hydrodynamic radius ∼ 0.5 nm), in 5P, 10P, 20P, and 50P PEG solutions, which have ξ varying between 3 and 0.5 nm (Table 1). The thermally fluctuating polymer network can confine the diffusion of fluorescein particles. The confinement ratio, given as $2R/\xi$ (R is the hydrodynamic radius of fluorescein), can vary from 0.3 to 1.86 as the polymer concentration is

https://doi.org/10.1021/acsomega.3c04917
ACS Omega 2023, 8, 35219−35231

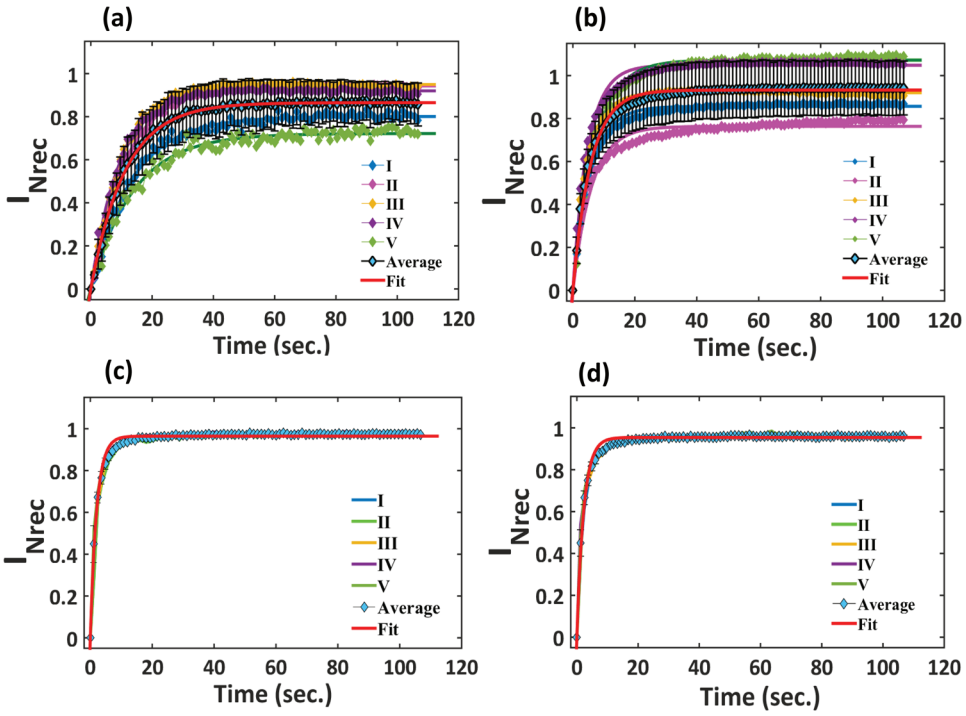

Figure 3. FRAP recovery curves of normalized fluorescence intensity I_{Nrec} as a function of time, for (a) 0.1 wt % bentonite in 20 wt % PEG solution, (b) 1 wt % bentonite in 20 wt % PEG solution, (c) 0.1 wt % CMC in 20 wt % PEG solution, and (d) 1 wt % CMC in 20 wt % PEG solution, after bleaching five different regions in the sample, with each region represented by Roman numerals I to V. From the data, the average (blue diamond symbols) is calculated, and error bars are calculated from the deviation of the curves from the average value. All curves are fits of data points with eq 3.

increased from 5P to 50P. As a control, the FRAP experiment performed for fluorescein diffusion in water yielded a fast fluorescein diffusion time and diffusion constant very close to the value predicted by the Stokes−Einstein relation (Figure 2a). Fluorescein diffuses fast in 5P solution too, with hardly any immobile fraction seen in the FRAP recovery curves (Figure 2b). Both the 5P and 10P solutions have similar recovery curves studied in different regions of the sample, so the error in the average recovery curve is negligible (Figure 2b,c). However, the 20P solution had comparatively more scatter in the recovery curves obtained for different regions of the sample, and hence comparatively larger errors in the average recovery, which could arise as a result of confined diffusion or inhomogeneities due to intermolecular bonding-induced structuring in PEG (Figure 2d). The maximum scatter was observed in the 50P recovery (Figure 2e), which was also slower. This points to the enhancement of confinement or microscale inhomogeneities as the polymer concentration is spanned through the semidilute to the concentrated regime. The recovery curves are fitted well with an exponential function, which gives the diffusion time (Figure 2a−e, Supporting Table S3), and diffusion constants (D) are obtained both from this diffusion time (eqs 4 and 5) and directly from the fit to eq 6 (Supporting Figure S1, Table S4). The D values obtained from the FRAP recovery curves are given in Table 2 for D3 (obtained from eq 5) and in Supporting Table S2 for D1 and D2 (obtained from eqs 4 and 6). For the control sample, eqs 5 and 6 resulted in values of D closer to the theoretical Stokes−Einstein value compared to eq 4. In all cases, the exponential function (eq 2, Figure 2a−e) fitted the data better than eq 6 (Supporting Figure S1). However, because of the presence of different types of interactions and structuring in the systems investigated, diffusion coefficients obtained from the $t_{1/2}$ values (Section 2.2) were used for comparison between different solutions rather than the diffusion time τ obtained from the experimental fits.

When bentonite particles are added to the 20P PEG solution, there is a reasonable scatter observed in the recovery curves in different regions of the sample probed (Figure 3a,b). Variability observed in the immobile fractions increased with bentonite concentration (Figure 3a,b). The D values obtained from the mean recovery data from five different regions of the sample are given in Table 2, whereas the D values of the sampled regions separately and their respective immobile fractions are given in Supporting Table S5. The heterogeneities in diffusion time and consequently the D values could arise due to several reasons—in the depletion zone, there are lesser polymer chains, and experiments and simulations have shown a marked inhomogeneity with respect to the actual polymer solution.[41−43] Surprisingly, although the diffusion time increased from that observed in 20P when 0.01 wt % bentonite was added, a marked decrease in diffusion time in 20P + 0.1B and 20P + 1B was observed compared to the 20P + 0.01B system, implying faster diffusion in these systems. Ideally, with an increase in bentonite concentration, the probes should experience more confinement and hindered diffusion with a larger diffusion time, but the contrary was observed. Moreover, D values from different scanned areas of the PEG + B solutions in the microchannel were observed to be heterogeneous. Control experiments with only bentonite in solution showed a faster diffusion (small τ) compared to the PEG + bentonite systems (Table 2, Supporting Figure S2, Table S2).

https://doi.org/10.1021/acsomega.3c04917
ACS Omega 2023, 8, 35219−35231

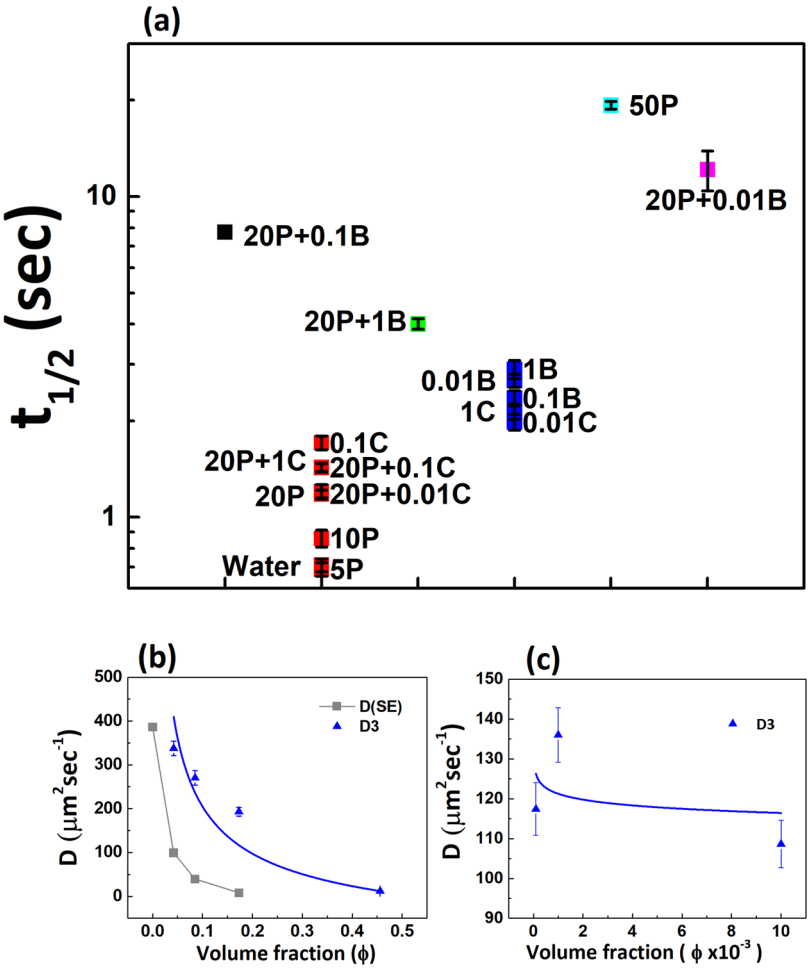

Figure 4. (a) Cluster graph of the diffusion half-time ($t_{1/2}$) of the fluorescein molecule in different polymer matrices with and without nanoparticles, illustrating the sensitive dependence of $t_{1/2}$ on the matrix structure. (b) Diffusion coefficient of fluorescein in the PEG matrix for different concentrations of PEG (D3), calculated with eq 5, as given in Table 2. The curve represents the fit to the nonentangled Rouse scaling $D \sim \varphi^{-0.54}$. The diffusion coefficients calculated with the Stoke−Einstein relation are also shown for comparison as the gray data, represented by D(SE). (c) Diffusion coefficients as a function of concentration for the pure CMC solution, which obey the pure polyelectrolyte scaling relation, $D \sim \varphi^{0}$, with D showing no definite trend as a function of concentration.

The mean D values for the 20P + 1B solution were found to be larger than the D values of 20P + 0.1B and 20P + 0.01B solutions, and the diffusion time was smaller. Comparatively high D values, or fast diffusion at the highest bentonite concentration studied, and detection of heterogeneities in diffusion time point to the presence of phase separation into polymer-rich and bentonite-rich phases. Hence, the D values obtained for different regions of the microchannel assess the diffusion in polymer-rich and bentonite-depleted subcompartments created due to the phase separation due to bentonite aggregation. Depletion interactions, mediated by the surrounding polymer chains, could be an important reason for this aggregation. Structural studies to analyze this aspect form the subject of a subsequent section. These observations illustrate that FRAP can be a sensitive estimate of the presence of phase-separated domains in the system. In fact, from the D values, it is clear that the phase separation commences right from the 20P + 0.1B system as it yields higher D values in different regions compared to the D values obtained in 20P + 0.01B. With an increase in bentonite concentration, depletion interactions play a crucial role in producing bentonite aggregation, which eventually leads to phase separation.

The immediate question that arises is what would the effects on microscale diffusion be if the nanoclay bentonite clusters are replaced by a reinforcing matrix of CMC polyelectrolytes, which are rigid polymers. It has been observed that aqueous solutions of NaCMC can have colloidally dispersed polyelectrolytes, or have networks and aggregates, depending on the degree of substitution (DS).[44,45] A SANS study by Lopez et al. found that NaCMC with DS = 1.2 is molecularly dissolved in water with a locally stiff conformation in the semidilute unentangled and entangled regimes, as well as the concentrated regime. They also found a tendency of weak aggregate formation due to the low q upturn of the scattering profiles.[45] In the present FRAP experiments, blends of NaCMC (DS = 0.7) of varying concentrations (0.01C, 0.1C, and 1.0C) with the 20P solution showed diffusion times similar to that observed in the 20P solution with very less scatter in the average profile, but a larger amount of immobile fraction compared to that observed in 20P was found in the 20P + CMC systems (Figure 3c,d, Table 2). This can arise either due to the presence of weak aggregates or weak PEG-CMC structural complexes or due to hindrance to the fluorescein diffusion due to confinement as a result of the semiflexible nature of CMC chains. When control experiments were

https://doi.org/10.1021/acsomega.3c04917
ACS Omega 2023, 8, 35219−35231

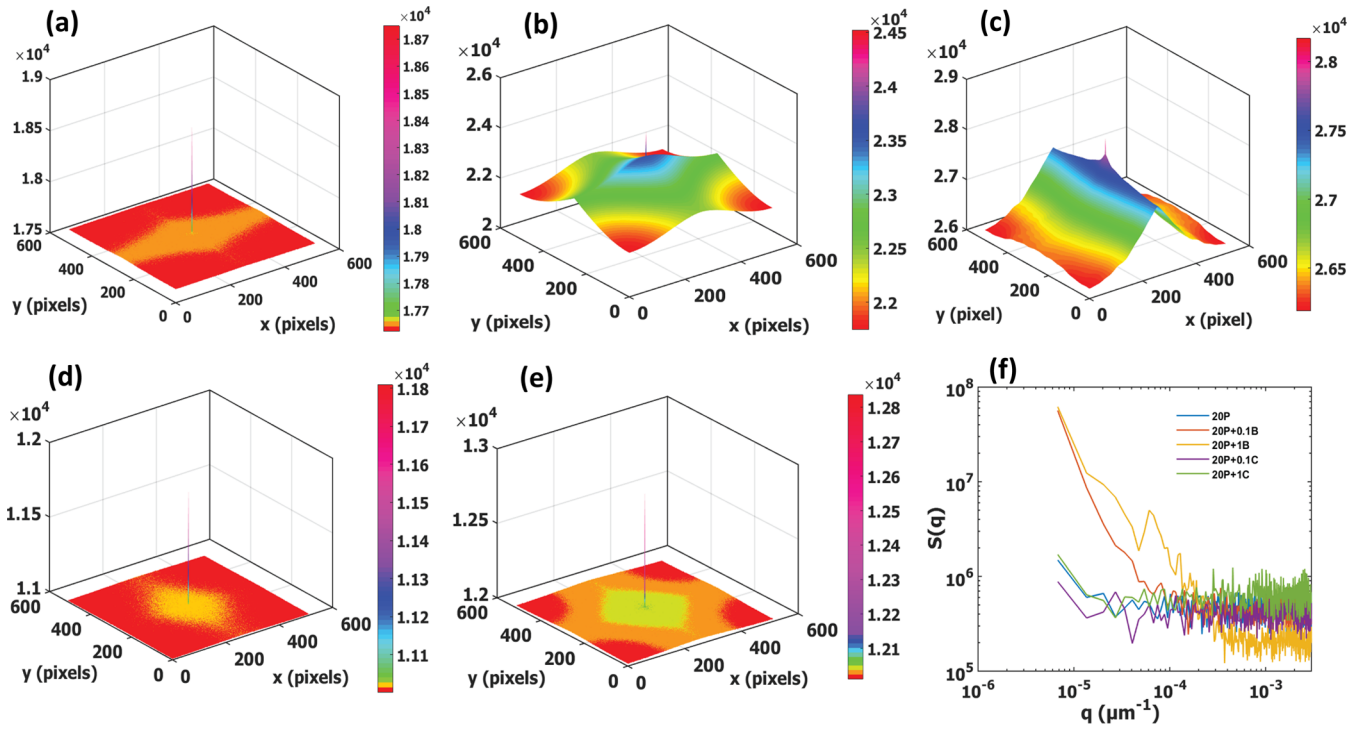

Figure 5. 2D spatial correlation functions for (a) 20 wt % PEG solution, (b) 20 wt % PEG + 0.1 wt % bentonite, (c) 20 wt % PEG + 1 wt % bentonite, (d) 20 wt % PEG + 0.1 wt % CMC solution, and (e) 20 wt % PEG + 1 wt % CMC solution, indicating longer-ranged correlations in solutions containing bentonite. (f) Static structure factor $S(Q)$ as a function of wave vector Q. In the case of solutions with bentonite, there is an enhancement of $S(Q)$ in the low Q region, indicating inhomogeneities or aggregates.

performed with an aqueous solution of only CMC, this immobile fraction was found to be greater than those observed in PEG + CMC solutions (Supporting Figure S2, Table 2), pointing to two possible reasons—presence of CMC aggregates and the topological hindrance to fluorescein diffusion by semiflexible CMC. The D values for aqueous CMC solutions in the present case seem to be similar to the fast mode D values obtained by dynamic light scattering experiments of CMC aqueous solutions, which also report additional slow and ultraslow modes of diffusion.[44] The fast mode of diffusion in ref 44 was independent of concentration, as we see in the present case, whereas the slow mode of diffusion was found to be strongly concentration-dependent.

Overall, a cluster analysis of the diffusion half-time $t_{1/2}$ shows that 10P and 5P cluster together with water, with 20P and 20P + 0.01C similar to this cluster (Figure 4a). However, the 20P blend with higher concentrations of CMC forms a separate cluster. This cluster has a lower $t_{1/2}$ compared to the cluster formed by 20P + 0.01B and 20P + 0.1B. 20P + 1B forms a separate cluster with a lower $t_{1/2}$ compared to the other PEG-bentonite solutions. Since there are several length scales present in the semidilute and concentrated PEG, PEG + B, and PEG + CMC, application of the Stokes−Einstein equation for the theoretical estimation of D can lead to improper values. For the PEG solutions, the mean D values follow Rouse scaling as a function of concentration (φ, in volume fraction) $D \sim \varphi^{-0.54}$ for $\varphi < 0.5$ (Figure 4b), whereas the solutions with only CMC have concentration-independent scaling of mean D values, with $D \sim \varphi^0$, the typical theoretical polyelectrolyte scaling (Figure 4c).

Large-scale molecular dynamics simulations of nanoparticle diffusivity of the polymer matrix reveal that the diffusion coefficient depends on the nanoparticle size as well as the polymer mesh size and polymer chain length.[46] If the nanoparticle size is smaller than the polymer entanglement mesh size, the simulation observed Rouse dynamics of polymer chains. If the entanglement mesh size decreases, the dynamics is no longer described by the Stokes−Einstein relationship.[46] In the present case, we observed Rouse dynamics and a strong departure from the Stokes−Einstein relationship. As the PEG concentration increases beyond 10P, it is evident from Table 1 that the size of the nanoparticles becomes comparable to the entanglement mesh size. Hence, it is not surprising that the D values calculated from the FRAP dynamics obey Rouse scaling. In addition, the results demonstrate that when the diffusivity of nanoparticles in a polymer network cannot be obtained by the Stokes−Einstein relationship, FRAP can give a convenient measure. D values obtained by FRAP sensitively demonstrate the presence of inhomogeneities in the polymer matrix. In order to validate this, a simultaneous measure of structuring in solution is needed. Hence, in the following section, we demonstrate a method of simultaneously obtaining a qualitative estimate of the solution structure detail from the prebleach fluorescence image and further verify it with solution small-angle X-ray and neutron scattering studies.

3.2. Structuring in PEG, PEG + Bentonite, and PEG + CMC Solutions. To study structural information arising from interactions in the systems investigated, two-dimensional correlation functions and the corresponding structure factors in the Fourier space were calculated for the PEG, PEG + cellulose, and PEG + bentonite solutions. Several groups have shown that by analyzing the intensity of microscope images in Fourier space, one can extract static as well as dynamic structure factors similar to the ones obtained in dynamic light scattering experiments.[38,39] Microscopy methods can provide structural information on a wider range of q values or length

https://doi.org/10.1021/acsomega.3c04917
ACS Omega 2023, 8, 35219−35231

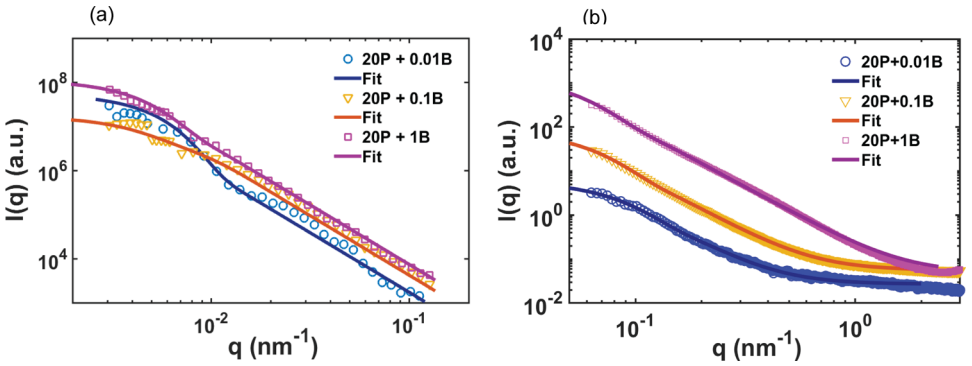

Figure 6. (a) MSANS and (b) SAXS intensity $I(q)$ as a function of the scattering wave vector q for 20P + 0.01 wt % bentonite, 20P + 0.1 wt % bentonite, and 20P + 1 wt % bentonite. The solid curves are fits to eq 9.

scales compared to dynamic light scattering. Moreover, highly concentrated solutions that become difficult to study by dynamic light scattering due to multiple scattering can be easily studied by microscope image analysis.

According to the convolution theorem, the Fourier transform of the correlation function or the convolution is the product of the Fourier transform of the image with the Fourier transform of its complex conjugate. Hence, the 2D autocorrelation function is obtained by an inverse Fourier transform of the convolution of the 2D images obtained by a confocal microscope using fluorescent molecular probes in the different solutions investigated in the previous sections (see Section 2.4). The results are shown in Figure 5a−e. Clearly, from this figure, the highest degree of correlation is found in the PEG-bentonite system as a result of enhanced structural interactions compared to PEG solutions or PEG + cellulose solutions. In the Q-space, the structure factor of PEG + bentonite also shows a low Q upturn, which implies the presence of inhomogeneities, arising due to the presence of bentonite aggregates (Figure 5f).

An analysis of the structure of the bentonite aggregates in PEG solution was carried out with medium-resolution small-angle neutron scattering (MSANS) and small-angle X-ray scattering (SAXS). The 20P + 0.01B MSANS data shows a small upturn at low q values, indicative of structuring in the solution (Figure 6a). As the bentonite concentration increases, the MSANS curves show a small increase in scattered intensity. As observed in Figure 6b, the SAXS intensity of the PEG solution is very small, but on addition of 0.1 wt % bentonite, there is a huge increase in the SAXS intensity, which gets further enhanced on increasing the bentonite concentration to 1 wt %. Nanoparticles have been observed to form hierarchical structures in a polymer matrix spreading over several length scales. Most often, these structures have fractal dimensions. The unified Guinier and power law model developed by Beaucage et al.[47−49] has been successfully applied for estimation of the hierarchical structures from small-angle scattering data. Estimation of several length scales in the hierarchical structuring requires wide-angle, small-angle as well as ultra-small-angle scattering data spanning several decades in the scattering wave vector, q. Considering the limited q range of the MSANS and SAXS data in Figure 6, each MSANS and SAXS curve separately yields one structural level of hierarchical structuring by fitting eq 9, the hierarchical fractal model for one structural level of cluster.

$$I(q) = I_a\left[\frac{\left\{\mathrm{erf}\left(\frac{qR_{ss}}{\sqrt{6}}\right)\right\}^3}{q/q_0}\right]^n + I_c\left[\exp\left(\frac{-q^2R_{ss}^2}{3}\right)\right] + I_o \quad (9)$$

The power law scaling exponent n can be related to the mass fractal dimension of the aggregates, whereas R_{ss} gives the size of the aggregates of bentonite discs. The normalization factor q_0 is taken to be $(q_{max} + q_{min})/2$, the average of the q range investigated. I_o is the scattering background. As is evident from Figure 6 and the fit results given in Table 3, eq 9 fits the experimental data very well (Red. χ^2 = 0.99), yielding two structural length scales for R_{ss} separately from the MSANS and the SAXS data. R_{ss} values obtained from SAXS give the size of bentonite nanoparticles. The large increase in forward scattering with an increase in bentonite concentration illustrates the enhancement in aggregate size with bentonite concentration. The presence of aggregates could not be probed in the CMC solutions because the scattering intensity detected had a very low signal-to-background ratio, similar to the PEG solution. It should be noted that the structure factor analysis in Figure 5 could hardly detect any structuring in CMC solutions, but in the case of bentonite solutions, the structure factors calculated from prebleach FRAP images also demonstrate the presence of aggregation, which sensitively increases with bentonite concentration.

Table 3. Results Obtained after Fitting the Model Denoted by eq 9 to the SAXS and MSANS Scattering Curves to Determine the Fractal Dimension (n) and Size of the Bentonite Aggregates (R_{ss}) for Various Concentrations of Bentonite in 20 wt % PEG

sample	n	R_{ss} (nm)	red. χ2
SAXS			
20P + 0.01B	2.8 ± 0.18	22 ± 0.3	0.99
20P + 0.1B	2.73 ± 0.07	29.3 ± 0.3	0.99
20P + 1B	2.7 ± 0.01	34.4 ± 0.3	0.99
MSANS			
20P + 0.01B	2.7 ± 0.2	360 ± 18	0.99
20P + 0.1B	2.69 ± 0.01	385 ± 172	0.98
20P + 1B	2.7 ± 0.1	410 ± 56	0.99

In order to investigate the presence of larger bentonite aggregates of a higher length scale than that probed by MSANS, phase contrast images of solutions were obtained. The bentonite concentration was fixed at 1%, and the polymer

https://doi.org/10.1021/acsomega.3c04917
ACS Omega 2023, 8, 35219−35231

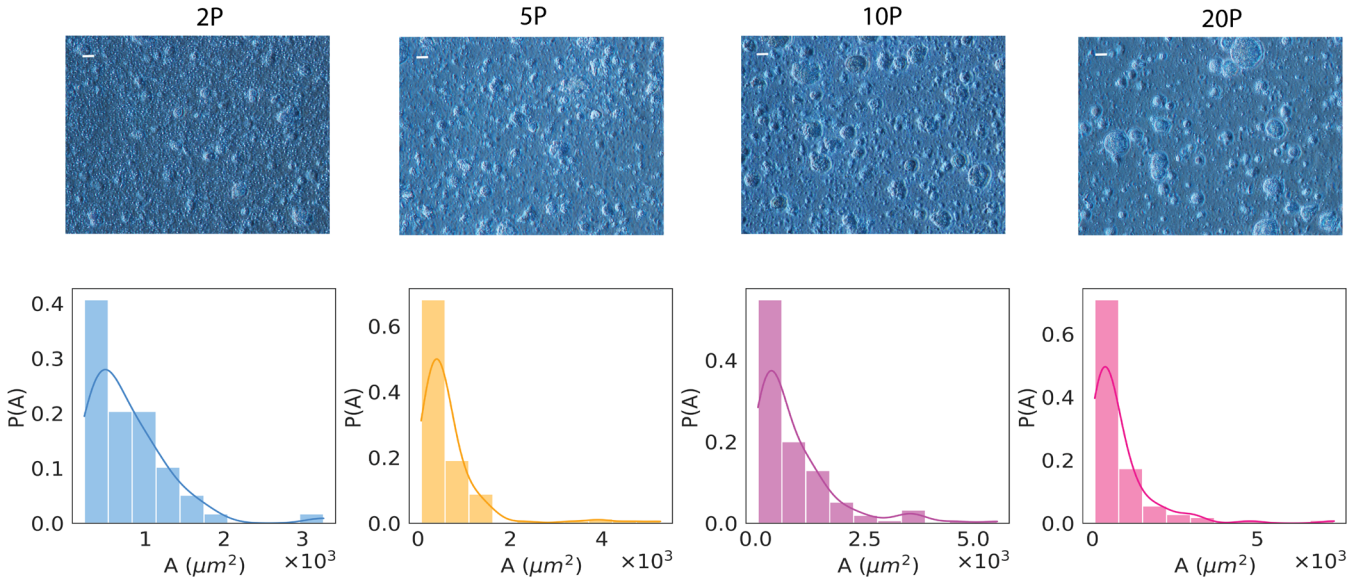

Figure 7. Phase contrast microscope images of bentonite structures with different concentrations of PEG—2P (2 wt %), 5P (5 wt %), 10P (10 wt %), and 20P (20 wt %)—in the aqueous solution (white scale bar = 10 μm) and the corresponding normalized histograms of the area of these structures. The histograms show the probability of occurrence of larger-sized bentonite aggregates as the PEG concentration is increased from 2 wt % (2P) to 20 wt % (20P) in 1 wt % bentonite. The area of the aggregates is denoted by A. The mean values of the bentonite aggregate size distributions are 724 ± 62 μm^2 for 2P, 682 ± 81 μm^2 for 5P, 868 ± 85 μm^2 for 10P, and 811 ± 107 μm^2 (10.2 ± 0.7 μm average aggregate size) for 20P solutions. Error bars have been calculated based on standard deviations from the mean.

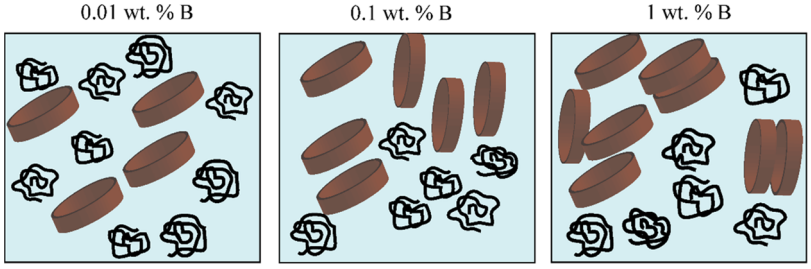

Figure 8. Schematic representation of microscale phase separation with an increase in bentonite nanoparticles (B, brown discs) in the PEG (black coils) matrix. At 1 wt % bentonite, bentonite-rich and PEG-rich clusters are very prominent.

concentration was increased from 2 to 20% (2P—20P). Phase contrast images and the corresponding particle size (area) histograms show evidence of enhanced flocculation of bentonite particles with an increase in polymer concentration (Figure 7). With an increase in polymer concentration, there are more nonadsorbed polymer chains, and this can result in entropic attractive depletion forces between bentonite particles. The size of the depletion zone is approximately equal to the radius of gyration of the polymer, and if two particles approach closer than twice the size of the depletion zone, then there is no polymer in the depletion zone (configurational distortion of the polymer in this small region leads to high entropic cost), and a net attractive force brings the bentonite particles together. The strength of the depletion force depends therefore on the concentration of the polymer solution, i.e., the osmotic pressure of the solution, and the range of the force depends on the size of the polymer molecule. Tuning this interaction has been found to yield interesting phase separation kinetics or the presence of long-lived metastable glassy and gel states in colloid−polymer mixtures.[17,22] In the PEG + bentonite matrix, the phase contrast images (Figure 7) show a propensity of phase-separated polymer-rich and bentonite-rich states with an increase in PEG concentration. The Asakura−Oosawa model gives an approximate estimation of the depletion interaction potential ($\varnothing_{Dep}$) in units of k_BT by $\frac{\varnothing_{Dep}}{k_BT} = -\frac{3b}{2R_g}\varphi$, where φ is the polymer volume fraction and b is the radius of the colloidal particle (≈34 nm for bentonite particles measured by SAXS).[50] With an increase in the polymer volume fraction, the depletion potentials vary from 0.5 k_BT for the 5P solution to 5 k_BT for the 50P solution (Table 1), implying that depletion interactions can lead to polymer-rich and bentonite-rich phases as the PEG concentration is increased. For 20P, the 2 k_BT depletion interaction, which tends to cause phase separation, can compete with the adsorption of PEG on a clay surface, which tends to form PEG-clay-associated structures, causing breakage of polymer-clay bridged networks. The moment there is an initiation of nucleation of the cluster, the radii of the bentonite clusters can be larger than the 34 nm value, producing a large increase in the value of $\varnothing_{Dep}$, driving the formation of more phase-separated domains. This can explain the phase separation in PEG-bentonite solutions with an increase in bentonite concentration (schematic in Figure 8). The FRAP experiments could effectively probe the diffusion kinetics and heterogeneities in the polymer-rich phase. When the phase separation kinetics proceed toward bentonite

https://doi.org/10.1021/acsomega.3c04917
ACS Omega 2023, 8, 35219−35231

aggregation, there is a decrease in the bentonite concentration with the spatially segregated polymer-rich phase, where the fluorescent probe has a smaller diffusion time. This explains the sudden decrease of diffusion time with bentonite concentration enhancement from 0.1 wt % onward.

Experimental studies have shown that the depletion layer around nanoparticle aggregates in polymer−nanoparticle composites has a nonuniform viscosity and leads to depletion-layer size-dependent values of diffusion coefficients.[41] A clear separation of slow and fast diffusion time scales arising due to the structure of the depletion layer has been observed.[41] In addition to the anomalies observed in nanoparticles with a spherical geometry, experimental studies of polymer diffusion in the presence of cylindrical-shaped nanoparticles like carbon nanotubes show nonlinear changes in diffusion coefficients with a change in nanoparticle concentration, favoring a trap model.[42] For chain diffusion in the presence of spherical nanoparticles, similarities with systems near glass transition and biological systems with molecular crowding have been observed.[42] In the case of nanoparticle diffusion, the bound polymer layer on the nanoparticle surface and the nanoparticle−polymer interaction have been found to play a role.[43] Hence, apart from depletion interactions, the nanoparticle aspect ratio or shape and nanoparticle−polymer interactions are some of the other parameters governing diffusion dynamics in polymer nanocomposites.

4. CONCLUSIONS

An important outcome of the present study is the demonstration that FRAP can be used to study diffusion in a polymer matrix at the microscale when the Stokes−Einstein relation fails. It also gives an idea of the structural inhomogeneities present, with diffusion time sensitively being altered by a phase separation kinetics proceeding in the direction of nanoparticle (bentonite) aggregation. The diffusion time estimates are homogeneous, with a very low scatter in the PEG + CMC systems, revealing one phase system. Thus, the effect of the presence of different types of fillers and the subsequent modifications in the polymer matrix, especially microscale mechanical modifications and matrix heterogeneity, is detected and analyzed. We have developed a novel way for obtaining qualitative microscale structuring details simultaneously with FRAP measurements using static Fourier space analysis of prebleach images. Microscale structuring in bentonite solutions is detected and quantified by MSANS, SAXS, and microscopy experiments at different structural length scales. Aggregation of bentonite particles can degrade the mechanical strength in applications that use clay filler particles in polymer solutions with the aim of enhancing the mechanical strength. Although aggregation is present in the microscale, it affects microscopic response, which, in turn, can affect properties at the macroscale, leading to inhomogeneities, microcracks, and phase instabilities. This is therefore a challenging problem that needs to be overcome. The diffusion time measurements presented here can thus be used in high-throughput material designing studies to obtain fast and reliable estimates of matrix heterogeneities in cases where fillers are added to improve mechanical properties.

ASSOCIATED CONTENT

Supporting Information

The Supporting Information is available free of charge at https://pubs.acs.org/doi/10.1021/acsomega.3c04917.

Measurements of diffusion coefficient (D) values in different in vitro and in vivo systems (Table S1); diffusion coefficient values (Table S2); fit parameters for exponential fit to the normalized recovery intensity (Table S3); fit parameters obtained on fitting the normalized recovery curves with eq 6 (Table S4); fits of the normalized recovery curves of an individual set of experiments with eq 5 on adding bentonite nanoparticles to 20P and for 20P for different regions of interest (Table S5); average FRAP recovery curves and their fits to eq 5 (Figure S1); and normalized recovery profiles on adding bentonite and CMC nanoparticles in 20P (Figure S2) (PDF)

AUTHOR INFORMATION

Corresponding Author

Debjani Bagchi − *Department of Physics, Faculty of Science, The Maharaja Sayajirao University of Baroda, Vadodara 390002 Gujarat, India;* orcid.org/0000-0003-1124-3051; Email: debjani.bagchi-phy@msubaroda.ac.in

Authors

Shipra Bhatt − *Department of Physics, Faculty of Science, The Maharaja Sayajirao University of Baroda, Vadodara 390002 Gujarat, India*

Avik Das − *Solid State Physics Division, Bhabha Atomic Research Centre, Mumbai 400085, India;* orcid.org/0000-0002-7770-4415

Ashwani Kumar − *Solid State Physics Division, Bhabha Atomic Research Centre, Mumbai 400085, India*

Debasis Sen − *Solid State Physics Division, Bhabha Atomic Research Centre, Mumbai 400085, India; Homi Bhabha National Institute, Mumbai 400094, India;* orcid.org/0000-0002-9080-0866

Complete contact information is available at: https://pubs.acs.org/10.1021/acsomega.3c04917

Author Contributions

The manuscript was written through contributions of all authors. All authors have given approval to the final version of the manuscript. S.B. and D.B. performed the experiments and analyzed the data; A.K. helped in SAXS data acquisition; A.D. performed the MSANS experiments; and D.B. conceived the project and acquired the necessary funding.

Notes

The authors declare no competing financial interest.

ACKNOWLEDGMENTS

The authors thank the Science and Engineering Research Board (SERB), New Delhi, for funding (EMR/2016/003910) and Dr. Feroz Musthafa, CCAMP, Bangalore, for confocal microscopy experiments. The authors also thank the Sophisticated Analytical Instrument Facility (SAIF), IIT Bombay, for preliminary small-angle X-ray scattering experiments.

REFERENCES

(1) Ekladious, I.; Colson, Y. L.; Grinstaff, M. W. Polymer−Drug Conjugate Therapeutics: Advances, Insights and Prospects. *Nat. Rev. Drug Discovery* **2019**, *18*, 273−294.

(2) Goktas, M.; Cinar, G.; Orujalipoor, I.; Ide, S.; Tekinay, A. B.; Guler, M. O. Self-Assembled Peptide Amphiphile Nanofibers and

PEG Composite Hydrogels as Tunable ECM Mimetic Microenvironment. *Biomacromolecules* **2015**, *16*, 1247−1258.
(3) Lin, C.-C.; Anseth, K. S. PEG Hydrogels for the Controlled Release of Biomolecules in Regenerative Medicine. *Pharm. Res.* **2009**, *26*, 631−643.
(4) Senapati, S.; Mahanta, A. K.; Kumar, S.; Maiti, P. Controlled Drug Delivery Vehicles for Cancer Treatment and Their Performance. *Signal Transduction Targeted Ther.* **2018**, *3*, No. 7.
(5) Xin, S.; Chimene, D.; Garza, J. E.; Gaharwar, A. K.; Alge, D. L. Clickable PEG Hydrogel Microspheres as Building Blocks for 3D Bioprinting. *Biomater. Sci.* **2019**, *7*, 1179−1187.
(6) Capanema, N. S. V.; Mansur, A. A. P.; de Jesus, A. C.; Carvalho, S. M.; de Oliveira, L. C.; Mansur, H. S. Superabsorbent Crosslinked Carboxymethyl Cellulose-PEG Hydrogels for Potential Wound Dressing Applications. *Int. J. Biol. Macromol.* **2018**, *106*, 1218−1234.
(7) Chang, C.-W.; Van Spreeuwel, A.; Zhang, C.; Varghese, S. PEG/Clay Nanocomposite Hydrogel: A Mechanically Robust Tissue Engineering Scaffold. *Soft Matter* **2010**, *6*, 5157−5164.
(8) Baghdadi, H. A.; Parrella, J.; Bhatia, S. R. Long-Term Aging Effects on the Rheology of Neat Laponite and Laponite−PEO Dispersions. *Rheol. Acta* **2008**, *47*, 349−357.
(9) Baghdadi, H. A.; Sardinha, H.; Bhatia, S. R. Rheology and Gelation Kinetics in Laponite Dispersions Containing Poly (Ethylene Oxide). *J. Polym. Sci., Part B: Polym. Phys.* **2005**, *43*, 233−240.
(10) Colby, R. H. Structure and Linear Viscoelasticity of Flexible Polymer Solutions: Comparison of Polyelectrolyte and Neutral Polymer Solutions. *Rheol. Acta* **2010**, *49*, 425−442.
(11) Daga, V. K.; Wagner, N. J. Linear Viscoelastic Master Curves of Neat and Laponite-Filled Poly (Ethylene Oxide)−Water Solutions. *Rheol. Acta* **2006**, *45*, 813−824.
(12) de Bruyn, J. R.; Pignon, F.; Tsabet, E.; Magnin, A. Micron-Scale Origin of the Shear-Induced Structure in Laponite−Poly (Ethylene Oxide) Dispersions. *Rheol. Acta* **2008**, *47*, 63−73.
(13) Schmidt, G.; Nakatani, A. I.; Han, C. C. Rheology and Flow-Birefringence from Viscoelastic Polymer-Clay Solutions. *Rheol. Acta* **2002**, *41*, 45−54.
(14) Bonn, D.; Denn, M. M.; Berthier, L.; Divoux, T.; Manneville, S. Yield Stress Materials in Soft Condensed Matter. *Rev. Mod. Phys.* **2017**, *89*, 35005.
(15) Divoux, T.; Tamarii, D.; Barentin, C.; Manneville, S. Transient Shear Banding in a Simple Yield Stress Fluid. *Phys. Rev. Lett.* **2010**, *104*, No. 208301.
(16) Pandey, R.; Conrad, J. C. Gelation in Mixtures of Polymers and Bidisperse Colloids. *Phys. Rev. E* **2016**, *93*, 12610.
(17) Weis, C.; Oelschlaeger, C.; Dijkstra, D.; Ranft, M.; Willenbacher, N. Microstructure, Local Dynamics, and Flow Behavior of Colloidal Suspensions with Weak Attractive Interactions. *Sci. Rep.* **2016**, *6*, No. 33498.
(18) Laurati, M.; Petekidis, G.; Koumakis, N.; Cardinaux, F.; Schofield, A. B.; Brader, J. M.; Fuchs, M.; Egelhaaf, S. U. Structure, Dynamics, and Rheology of Colloid-Polymer Mixtures: From Liquids to Gels. *J. Chem. Phys.* **2009**, *130*, No. 134907.
(19) Takeda, M.; Matsunaga, T.; Nishida, T.; Endo, H.; Takahashi, T.; Shibayama, M. Rheo-SANS Studies on Shear Thickening in Clay−Poly (Ethylene Oxide) Mixed Solutions. *Macromolecules* **2010**, *43*, 7793−7799.
(20) Amin, D.; Wang, Z. Nonlinear Rheology and Dynamics of Supramolecular Polymer Networks Formed by Associative Telechelic Chains under Shear and Extensional Flows. *J. Rheol.* **2020**, *64*, 581−600.
(21) Denton, A. R. Nonlinear Screening and Effective Electrostatic Interactions in Charge-Stabilized Colloidal Suspensions. *Phys. Rev. E* **2004**, *70*, 031404.
(22) Eckert, T.; Bartsch, E. Re-Entrant Glass Transition in a Colloid-Polymer Mixture with Depletion Attractions. *Phys. Rev. Lett.* **2002**, *89*, No. 125701.
(23) García, Á. G.; Tuinier, R. Tuning the Phase Diagram of Colloid-Polymer Mixtures via Yukawa Interactions. *Phys. Rev. E* **2016**, *94*, 062607.
(24) Park, N.; Rathee, V.; Blair, D. L.; Conrad, J. C. Contact Networks Enhance Shear Thickening in Attractive Colloid-Polymer Mixtures. *Phys. Rev. Lett.* **2019**, *122*, No. 228003.
(25) Ruiz-Franco, J.; Camerin, F.; Gnan, N.; Zaccarelli, E. Tuning the Rheological Behavior of Colloidal Gels through Competing Interactions. *Phys. Rev. Mater.* **2020**, *4*, 45601.
(26) Trappe, V.; Weitz, D. A. Scaling of the Viscoelasticity of Weakly Attractive Particles. *Phys. Rev. Lett.* **2000**, *85*, 449.
(27) Kang, M.; et al. Simplified Equation to Extract Diffusion Coefficients from FRAP Data. *Traffic* **2012**, *13*, 1589−1600.
(28) Kang, M.; Andreani, M.; Kenworthy, A. K. Validation of Normalizations, Scaling, and Photofading Corrections for FRAP Data Analysis. *PLoS One* **2015**, *10*, No. e0127966.
(29) Wu, J.; Shekhar, N.; Lele, P. P.; Lele, T. P. FRAP Analysis: Accounting for Bleaching during Image Capture. *PLoS One* **2012**, *7*, No. e42854.
(30) Bläßle, A.; Soh, G.; Braun, T.; Mörsdorf, D.; Preiß, H.; Jordan, B. M.; Müller, P. Quantitative Diffusion Measurements Using the Open-Source Software PyFRAP. *Nat. Commun.* **2018**, *9*, No. 1582.
(31) Axelrod, D.; Koppel, D. E.; Schlessinger, J.; Elson, E.; Webb, W. W. Mobility Measurement by Analysis of Fluorescence Photobleaching Recovery Kinetics. *Biophys. J.* **1976**, *16*, 1055−1069.
(32) Blumenthal, D.; Goldstien, L.; Edidin, M.; Gheber, L. A. Universal Approach to FRAP Analysis of Arbitrary Bleaching Patterns. *Biophys. J.* **2015**, *108*, No. 77a.
(33) Guinier, A.; Fournet, G.; Walker, C. B.; Yudowitch, K. L.*Small-Angle Scattering of X-Rays*; Wiley: New York, 1955.
(34) Glatter, O.; Kratky, O. *Small Angle X-Ray Scatt. Sch.*; Academic Press: London, UK, 1982.
(35) Mazumder, S.; Sen, D.; Saravanan, T.; Vijayaraghavan, P. R. Performance and Calibration of the Newly Installed Medium Resolution Double Crystal Based Small-Angle Neutron Scattering Instrument at Trombay. *J. Neutron Res.* **2001**, *9*, 39−57.
(36) Mazumder, S.; Sen, D.; Saravanan, T.; Vijayaraghavan, P. R. A Medium Resolution Double Crystal Based Small-Angle Neutron Scattering Instrument at Trombay. *Curr. Sci.* **2001**, *81*, 257−262.
(37) Das, A.; Bahadur, J.; Kumar, A.; Sen, D. Performance of Small- and Wide-Angle x-Ray Scattering Beamline at Indus-2 Synchrotron. *Rev. Sci. Instrum.* **2023**, *94*, No. 043902.
(38) Aime, S.; Cipelletti, L. Probing Shear-Induced Rearrangements in Fourier Space. II. Differential Dynamic Microscopy. *Soft Matter* **2019**, *15*, 213−226.
(39) Cerbino, R.; Trappe, V. Differential Dynamic Microscopy: Probing Wave Vector Dependent Dynamics with a Microscope. *Phys. Rev. Lett.* **2008**, *100*, No. 188102.
(40) Furukawa, R.; Arauz-Lara, J. L.; Ware, B. R. Self-Diffusion and Probe Diffusion in Dilute and Semidilute Aqueous Solutions of Dextran. *Macromolecules* **1991**, *24*, 599−605.
(41) Ziębacz, N.; Wieczorek, S. A.; Kalwarczyk, T.; Fiałkowski, M.; Hołyst, R. Crossover Regime for the Diffusion of Nanoparticles in Polyethylene Glycol Solutions: Influence of the Depletion Layer. *Soft Matter* **2011**, *7*, 7181−7186.
(42) Goswami, M.; Sumpter, B. G. Anomalous Chain Diffusion in Polymer Nanocomposites for Varying Polymer-Filler Interaction Strengths. *Phys. Rev. E* **2010**, *81*, 41801.
(43) Griffin, P. J.; Bocharova, V.; Middleton, L. R.; Composto, R. J.; Clarke, N.; Schweizer, K. S.; Winey, K. I. Influence of the Bound Polymer Layer on Nanoparticle Diffusion in Polymer Melts. *ACS Macro Lett.* **2016**, *5*, 1141−1145.
(44) Behra, J. S.; Mattsson, J.; Cayre, O. J.; Robles, E. S. J.; Tang, H.; Hunter, T. N. Characterization of Sodium Carboxymethyl Cellulose Aqueous Solutions to Support Complex Product Formulation: A Rheology and Light Scattering Study. *ACS Appl. Polym. Mater.* **2019**, *1*, 344−358.
(45) Lopez, C. G.; Rogers, S. E.; Colby, R. H.; Graham, P.; Cabral, J. T. Structure of Sodium Carboxymethyl Cellulose Aqueous Solutions: A SANS and Rheology Study. *J. Polym. Sci., Part B: Polym. Phys.* **2015**, *53*, 492−501.

https://doi.org/10.1021/acsomega.3c04917
ACS Omega 2023, 8, 35219−35231

(46) Yamamoto, T.; Masubuchi, Y.; Doi, M. Relaxation Dynamics of the Normal Stress of Polymer Gels. *Macromolecules* **2017**, *50*, 5208−5213.
(47) Beaucage, G.; Schaefer, D. W. Structural Studies of Complex Systems Using Small-Angle Scattering: A Unified Guinier/Power-Law Approach. *J. Non-Cryst. Solids* **1994**, *172-174*, 797−805.
(48) Beaucage, G. Approximations Leading to a Unified Exponential/Power-Law Approach to Small-Angle Scattering. *J. Appl. Crystallogr.* **1995**, *28*, 717−728.
(49) Takenaka, M. Analysis of Structures of Rubber-Filler Systems with Combined Scattering Methods. *Polym. J.* **2013**, *45*, 10−19.
(50) Asakura, S.; Oosawa, F. Interaction between Particles Suspended in Solutions of Macromolecules. *J. Polym. Sci.* **1958**, *33*, 183−192.
(51) Linegar, K. L.; Adeniran, A. E.; Kostko, A. F.; Anisimov, M. A. Hydrodynamic Radius of Polyethylene Glycol in Solution Obtained by Dynamic Light Scattering. *Colloid J.* **2010**, *72*, 279−281.

https://doi.org/10.1021/acsomega.3c04917
ACS Omega 2023, 8, 35219−35231